Article:
Lopez Dubon, S. orcid.org/0000-0003-0663-607X, Cuthill, F., Vogel, C. orcid.org/0000-0003-2232-9811 et al. (2 more authors) (2024) A full-scale composite tidal blade fatigue test using single and multiple actuators. Composites Part A: Applied Science and Manufacturing, 181. 108140. ISSN 1359-835X

https://doi.org/10.1016/j.compositesa.2024.108140

Composites: Part A 181 (2024) 108140

Contents lists available at ScienceDirect

Composites Part A

journal homepage: www.elsevier.com/locate/compositesa

A full-scale composite tidal blade fatigue test using single and multiple actuators

Sergio Lopez Dubon [a,*], Fergus Cuthill [a], Christopher Vogel [b], Conchur Ó Brádaigh [c], Edward D. McCarthy [a]

[a] The University of Edinburgh, Edinburgh, EH8 9YL, Scotland, United Kingdom
[b] University of Oxford, Oxford, OX1 3PJ, England, United Kingdom
[c] The University of Sheffield, Sheffield, S10 2TN, England, United Kingdom

ARTICLE INFO

Keywords:
Fatigue
Composite tidal blades
Testing

ABSTRACT

In order to perform fatigue testing on tidal turbine blades, it is necessary to apply cyclic loads that do not match the blade's natural frequency. This is due to the high stiffness of the blades and the thermal challenges associated with testing composite materials at frequencies typically around 18–20 Hz. To overcome this challenge, auxiliary systems are used to load the blades. However, conventional hydraulic systems commonly used for this purpose are known to be energy-intensive and inefficient. In this work, we present results obtained at the FastBlade fatigue testing facility, which utilises a regenerative digital displacement hydraulic pump system to address these issues. This innovative system has proven to be highly efficient, resulting in up to 75% energy savings compared to standard hydraulic systems. To perform these tests, we first performed a series of Reynolds-Averaged Navier–Stokes (RANS) simulations using on-site water velocity data to determine equivalent target hydrodynamic loads. These target loads are applied to the blades using initially a single contact point and, later, three load contact points. The FastBlade facility showcases an effective approach to fatigue testing during these tests. Throughout the testing process, comprehensive measurements are taken to evaluate the response of the blades and the FastBlade test structure itself. These measurements provide valuable insights into the mechanical behaviour of the blades when a single or multi-actuator setup is used to match the root bending moment and contribute to the refinement of testing practices. Notably, the blades successfully endured the equivalent of 20 years of tides in an accelerated fatigue loading test without experiencing catastrophic failure. The data obtained from these tests will enable the identification of improvements in testing procedures, including control strategies, load introduction methods, instrumentation layout, instrument calibration, and test design. This knowledge will lead to enhanced performance and reliability of the FastBlade facility, further advancing the field of tidal turbine blade testing.

1. Introduction

The tidal energy industry has a long history and has attracted renewed interest in recent years. The first tidal developments consisted of tidal lagoons and barrages (i.e., La Rance, France, 1967) and, whereas more recently, less invasive systems such as stream tidal turbines have been developed [1,2]. The industry has started to grow globally, particularly in the UK [3–5], with many different devices and prototypes developed in the past few years; see [4] for further details.

Tidal and wave energy sources have the potential to make a significant contribution to the EU power grid by generating 100 GW of power by 2050, which could supply a third of EU homes and drive economic activity and job creation [6]. Horizontal axis turbines (HATs) are vital for developing tidal stream energy. However, designing HATs poses challenges as they operate in seawater, which is 800 times denser than air and exerts significantly higher loads per unit blade span. Existing designs of tidal turbine blades are based on blade element momentum theory and simplified Finite Element Models [7–9]. The demanding fluid conditions in which tidal turbine blades operate result in high-stress concentrations, increasing the risk of fatigue failure over their 20-year design life. The limited data and understanding of fatigue in tidal blades lead to conservative blade designs and higher levelized costs of energy (LCOE) compared to other renewable energy technologies [10]. To mitigate the risk of turbine blade fatigue failure

* Corresponding author.
E-mail address: Sergio.LDubon@ed.ac.uk (S. Lopez Dubon).

https://doi.org/10.1016/j.compositesa.2024.108140
Received 19 December 2023; Received in revised form 8 March 2024; Accepted 9 March 2024
Available online 12 March 2024

and reduce LCOE, there is a renewed focus on improving test methods, obtaining more representative data, and developing new design methodologies.

Nevertheless, much of the information regarding the blade design and performance remains an industrial secret, with the available information usually restricted to the length of the blades and the overall energy production, which includes the impacts of other aspects of the tidal device, such as drive train losses and not just the blade performance. One of the few in situ holistic turbine performance experiments was made by [11], who evaluated scale models under real sea conditions, and [12], who measured (with strain gauges) the loads on a tidal blade at Connel, Scotland. More recently, in situ, information on array performance has been collected rather than for a single device (i.e., [13]).

In situ tests are complex, and not all environmental conditions can be controlled. Furthermore, the test is subjected to a set of actual conditions that may exclude extreme events important for determining the maximum load cases. The exposure time is generally longer compared to laboratory conditions, but crucially does not necessarily result in the sufficiently high load intensities needed to instil confidence in structural performance. Lastly, in situ environmental measurements are much less straightforward to take than in a laboratory environment. Nevertheless, it is clear that laboratory conditions cannot fully replicate some of the complicated conditions and interactions encountered offshore. Therefore, a common practice is performing onshore laboratory testing first and then moving the prototype to in situ testing.

The hydrodynamic testing facilities for scale models are more developed than structural facilities. Typically, hydrodynamic tests are done in flumes to investigate the hydrodynamic performance of the blade after a numerical optimisation (i.e., [14–17]), or in turbine farms [18]. Examples include the use of wave-towing tanks for hydrodynamic validations [19–24], and the circulating water channel of Harbin Institute of Technology, Weihai [25]. The optimisation and test of a 300 W counter-rotating type horizontal axis tidal turbine was carried out on a rotating arm tank at Shanghai Shipping Research Institute [26]. Cavitation tests are also performed, c.f., the Emerson cavitation tunnel at Newcastle University [27,28], and the cavitation tunnel of Shanghai Shipping Research Institute [29]. There have also been experiments outside water using wind tunnels to evaluate pitch angles [30–32]. One of the most exciting facilities is FloWave, which is a circular combined wave and current test tank at the University of Edinburgh that can produce multi-directional waves and currents [33], allowing the measurement of loads under different wave and current conditions [34–39].

Recent advancements in full-scale fatigue testing of composite material tidal blades include a 2018 test conducted at the University of Galway, where a 3/8th scale blade designed by OpenHydro underwent testing, achieving a maximum load amplitude of 35 kN and 275,000 cycles [40]. In 2020, a new turbine blade fatigue test standard, IEC TS 62600-3:2020, was published [41]. The FastBlade facility was inaugurated at the Port of Rosyth, Scotland, in 2022, enabling accelerated lifetime fatigue testing of full-scale tidal blades and other elongated structures [42–44]. In the same year, the University of Galway performed another fatigue test involving two full-scale blades measuring 2 and 3 m in length from SCHOTTEL HYDRO. The 2 m blade endured a maximum load of 6.9 kN over 150,000 cycles at 0.3 Hz, while the 3 m blade experienced a maximum load of 14 kN over 16,000 cycles at 0.1 Hz [45]. The authors also conducted a three-actuator test for static loads at high load levels, following the standard IEC TS 62600-3:2020. Subsequently, fatigue testing was performed at low load levels with an increased number of cycles up to 300,000, adhering to the DNVGL-ST-0164 standard [46], and a final static test was conducted [47]. More information about the tests developed in this facility can be found in [48].

In 2022, the FastBlade facility conducted the first high load fatigue test, reaching a Root Bending Moment (RBM) of 652 kN A m and operating at a high frequency of 1 Hz, in accordance with the IEC TS 62600-3:2020 standard. The test consisted of 31,775 cycles, equivalent to approximately 21.7 years of tidal cycles. Remarkably, the blade exhibited no catastrophic failure or significant changes in stiffness over the test [42,43]. This study investigates the use of three actuators and examines the blade's response by repeating the test conducted in FastBlade in 2022 using the same blade [42,43]. Moreover, these FastBlade tests show that it is possible to accelerate a fatigue test while retaining the same strain values [44].

2. Method

2.1. Site data

The flow data used in this project were obtained from the ReDAPT project conducted at the Fall of Warness, European Marine Energy Centre (EMEC), Orkney, UK. The data were collected using two acoustic Doppler current profilers deployed between July 19th and August 2nd 2013, 0.8 m above the seabed [49–51]. The profilers sampled the flow at a frequency of 0.5 Hz. The mean operating depths were 43.2 m and 46.2 m, respectively, due to slight variations in seabed conditions at the different locations.

For data analysis, the flow speed and turbulence intensity values were categorised into specific bins of hub-height mean flow speed (U_∞) for both flood and ebb tides. The bins were defined as U_∞ = (0.7,1.4,2.1,2.8,3.0,3.5) m/s, with the highest value of U_∞ = 3.5 m/s observed exclusively during ebb tide. Measurements were considered only when the wave height was below 1 m to ensure data quality. A 5-minute ensemble length was used for all statistical analyses, and a turbulence intensity noise correction estimate of 0.12 cm/s was applied following the procedure outlined in [50].

2.2. Computational fluid dynamics model

The unsteady Reynolds-Averaged Navier–Stokes (URANS) simulations in this study were performed using the computational fluid dynamics (CFD) solver OpenFOAM (version 2.3.1). The choice of URANS simulation was based on previous work [52], which showed that URANS and Large Eddy Simulation produce similar results for phase-averaged loads and blade pressure distributions in low onset turbulence flows, which is the focus of this paper. The PimpleFoam PISO algorithm was employed for the simulations, and the turbulence closure was provided by the $k-\omega$ SST model with the 2003 updated coefficients [53]. Each simulation ran for a duration of 400 s, with a time step of 0.03 s.

The computational domain used in this study had dimensions of 250 m in length, 520 m in width, and 43 m in height, matching the height of the ReDAPT site. The width of the domain was set to achieve a small geometric blockage ratio of 1.14%. At the inlet of the computational domain, a vertical flow profile was imposed using the atmospheric boundary layer inlet condition available in OpenFOAM. The flow profile was sustained by a no-slip wall boundary condition at the bottom of the domain and a stress boundary condition at the top. The outlet boundary had a fixed static pressure of 0 Pa, and zero gradient boundary conditions were applied to the turbulence and velocity scalars. Symmetry conditions were used on the lateral boundaries. The inflow and top boundary conditions were adjusted to match the observed flow profile from the ReDAPT data.

An Octree mesh with three levels of grid refinement was employed to discretise the computational domain. The mesh parameters were evaluated for convergence and found to be in good agreement with field observations using a homogeneous grid dimension of 1.5 m. Two additional levels of refinement were implemented near the rotor and in the wake region, resulting in a mesh with approximately 2.8×10^6 elements. The turbine was emulated using the actuator line method, eliminating the need for rotating sub-domains or mesh interfaces and

reducing computational costs. However, the mesh was refined in the vicinity of the turbine to capture the significant velocity gradients around the blades.

The actuator line method was utilised to represent the turbine blades, where each blade was represented by a rotating line along which forces were applied to the flow [54,55]. Blade forces were calculated using 2D blade element theory with 100 collocation points. The flow field around each blade was sampled using the potential flow equivalence method and reintroduced using the Gaussian smearing technique. The calculated blade forces were adjusted using the tip loss model proposed by Shen et al. [56] to account for the $3D$ flow effects that reduce the blade forces near the tips. The turbine nacelle was represented using a cell-blocking method to enforce zero velocity and allow impermeable bodies to be included in the numerical domain without explicit geometry resolution [57]. The model has been validated against reference turbines; for further details, see, e.g. [54,55].

3. Experiment setup

Once the loads were defined, the mechanical test campaign with one and three actuators followed the IEC TS 62600-3:2020 standard [41] by performing the following test sequence: 1st, a static test; 2nd, a fatigue test; and 3rd, a static test. Before the three-actuator testing phase at FastBlade, the blade had previously undergone a single actuator test. It was determined that the blade's centre of gravity is located at 900 ± 30 mm from the root, and the weight of the blade is 1588.59 kg (15584.07 N). With a single actuator, the natural frequency tests showed a slight reduction in natural frequency of 0.54% from 18.0278 Hz to 17.9308 Hz at the end of the test campaign, indicating minimal damage [58], and allowing the performance of the three actuator test.

3.1. Specimen information

The tidal turbine blade (see Fig. 1) was designed by Tidal Generation Limited and manufactured by Aviation Enterprises Limited as part of the DeepGen tidal project. It was obtained from a decommissioned 500 kW tidal stream turbine previously installed at EMEC's test site at the Fall of Warness for approximately two years. The extent of any damage or deterioration the blade suffered during the in-situ test at EMEC is unclear. Unfortunately, FastBlade did not receive some design documents, which were lost and unavailable. The company responsible for the blade design no longer exists; another company acquired the rights (Airborne).

The blade's cross-section is based on the NACA 63-4XX aerofoil series, where XX represents the thickness-to-chord ratio ranging from 55% at the root to 18% at the tip. The innermost section of the blade features a cylindrical cross-section with an implied thickness-to-chord ratio of 100%. The lift and drag characteristics of the aerofoil, as a function of the angle of attack, were computed using QBlade [59], considering a chord-based Reynolds number range of $1.0 \times 10^7 < Re < 1.8 \times 10^7$ and a critical number Ncrit = 9 for all cases. NACA aerofoil coordinates were determined by using 300 equally spaced points [60].

The blade has an 8 mm-thick glass fibre skin, while pairs of 3 mm thick glass fibre ribs are used for additional stiffness. The spar cap is made of 75% unidirectional carbon fibre epoxy prepreg, with the shear webs consisting of ±45° carbon fibre epoxy prepreg. A rear glass fibre epoxy spar is present, connecting the suction and pressure sides, situated 100 mm away from the trailing edge to alleviate peel stresses at the trailing edge [62].

Table 1
Strong wall capability at FastBlade.

Load capacity	Moment (MN m)	Shear (MN)
Fatigue (400 million cycles pushing)	4.70	0.94
Fatigue (400 million cycles Pulling)	4.70	0.94
Static (Quasi-static load Pulling)	11.96	2.39
Static (Quasi-static load Pushing)	10.74	2.13

Table 2
Characteristics of the longitudinal lines.

No.	Description
1	Topside in line with XB axis
2	Topside in line with YB axis
3	Left-side follows leading edge
4	Bottom side in line with XB axis
5	Topside follows the trailing edge.

3.2. Facility description

FastBlade is equipped with a robust 70-tonne reaction frame capable of withstanding substantial loads during static and fatigue testing, as detailed in Table 1. Furthermore, it features a reversible hydraulic flow rate of 880 litres per minute.

The FastBlade structure comprises a reaction plane, support wall, T-Slot bed plates, and an adapter plate. It is securely positioned on bridge bearings and situated within a 2.5 m pit on the floor, as depicted in Fig. 2. The hydraulic system of FastBlade employs four Digital Displacement hydraulic reversible pumps developed by Danfoss. These pumps enable the system to recover the energy utilised during testing. Notably, this hydraulic system consumes up to 75% less energy than hydraulic systems of similar size at high loads. Furthermore, it provides precise control over the actuators, facilitating the implementation of compound loads that more accurately simulate complex ocean interactions.

3.3. Setups

In the test setup, the data collection system incorporates a range of sensors, including load cells, accelerometers, linear position sensors, strain gauges, thermocouples, and linear string potentiometers. The Flex-logger software controls the entire data collection process. In this paper, the focus is on the data obtained from the strain gauges and displacement sensors, precisely positioned along line one in the horizontal direction edgewise direction (ZB) for both the top and bottom sections of the blade, as illustrated in Fig. 3.

The selection of the loading direction for the test was based on the findings of [62]. According to the results, the single actuator was positioned at 3.56 m from the root of the blade and, for the three actuators test, the actuators were placed at distances of 2.26, 3.56, and 4.48 m, respectively, from the back face of the blade connection flange. These were identified as the optimal locations in order to maximise the similarity between the hydrodynamic results and the mechanical test for the bending moment distribution. The loads were applied in the XBB direction, effectively generating the desired moment around the YBB axis. This configuration is illustrated in Fig. 4.

The longitudinal lines in Fig. 4 go from the root to the tip of the blade, and the description is presented in Table 2. The transverse coordinates along the blade are established as lines projected around the blade at specific distances from and running parallel to the root connection. The initial transverse line, denoted as Line 1, is positioned 900 mm from the root, with subsequent lines uniformly spaced at 800 mm intervals. Moreover, the coordinates of the sensors are determined by specifying the transverse line first, followed by the longitudinal line they occupy.

A configuration consisting of clamped wooden saddles with a steel frame and a 1.5 mm thick silicone sheet at the blade interface was

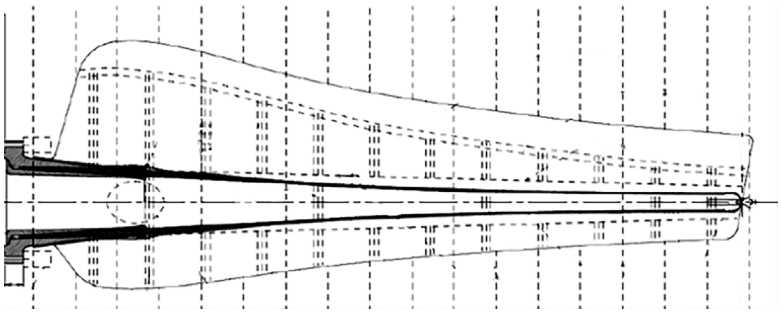

Fig. 1. Top view of the blade from a technical drawing from [61].

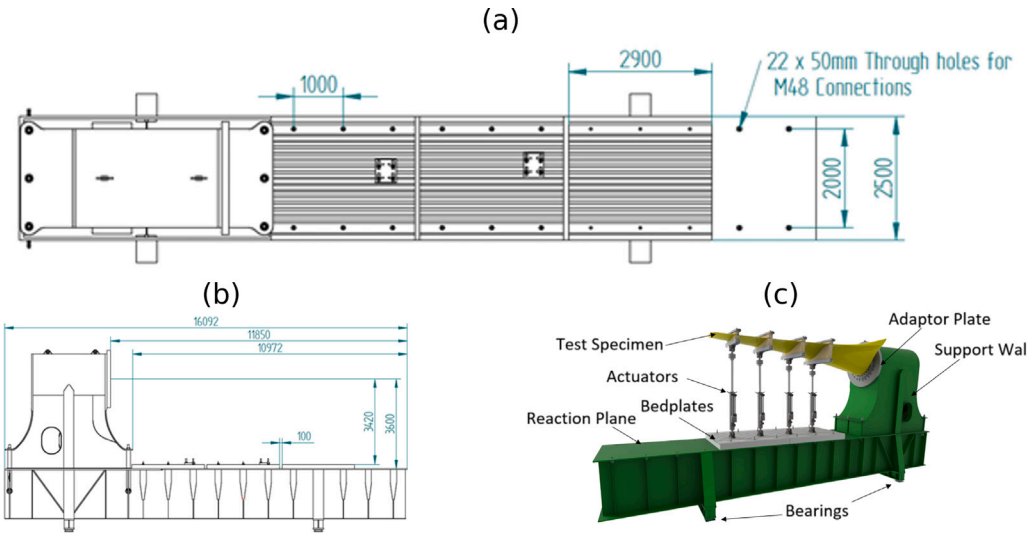

Fig. 2. General arrangement and dimensions of the reaction frame at FastBlade. (a) Top view; (b) Lateral view; and (c) General view.

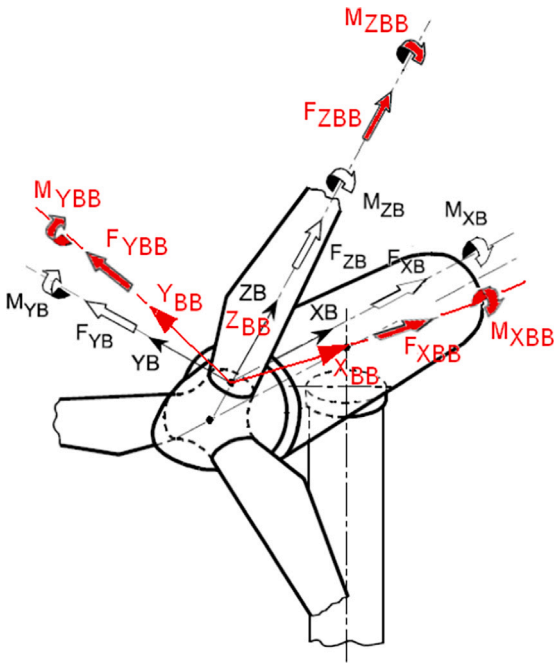

Fig. 3. Blade's coordinate system.

utilised to introduce the loads. The detailed analysis of the stresses induced by the clamping system is still ongoing. However, initial findings from the DIC system indicate that these stresses are insignificant compared to those resulting from the applied loads. Fig. 5 provides a visual representation of the final configuration of the system for each of the tests.

4. Results

4.1. Hydrodynamics

The study conducted simulations of the rotor at different flow speeds during flood and ebb tides. The performance of the rotor varied due to differences in velocity shear profiles between the tides, even when the hub-height velocity was the same. The analysis focused on spanwise axial and tangential blade loads, which generally increased along the blade as the incident flow speed increased, as shown in Fig. 6. The mean blade loads were slightly higher for the rotor during the ebb tide, primarily because of a more significant velocity shear across the rotor's swept area. These factors caused the rotor to operate further away from its hydrodynamic optimum, resulting in an increased spread between the minimum and maximum blade loads, particularly in the lower part of the rotation.

The simulations demonstrated that the blade loads, overall power, and thrust exhibited fluctuations caused by the rotational sampling of the shear profile by the blades. This resulted in azimuthal variations in blade root bending moments. The normalised root bending moments (RBMs) were higher for the rotor operating in the ebb tide between 90–270°. However, the higher RBMs during the flood tide countered this effect in the upper half of the blade rotation (refer to Fig. 7). The

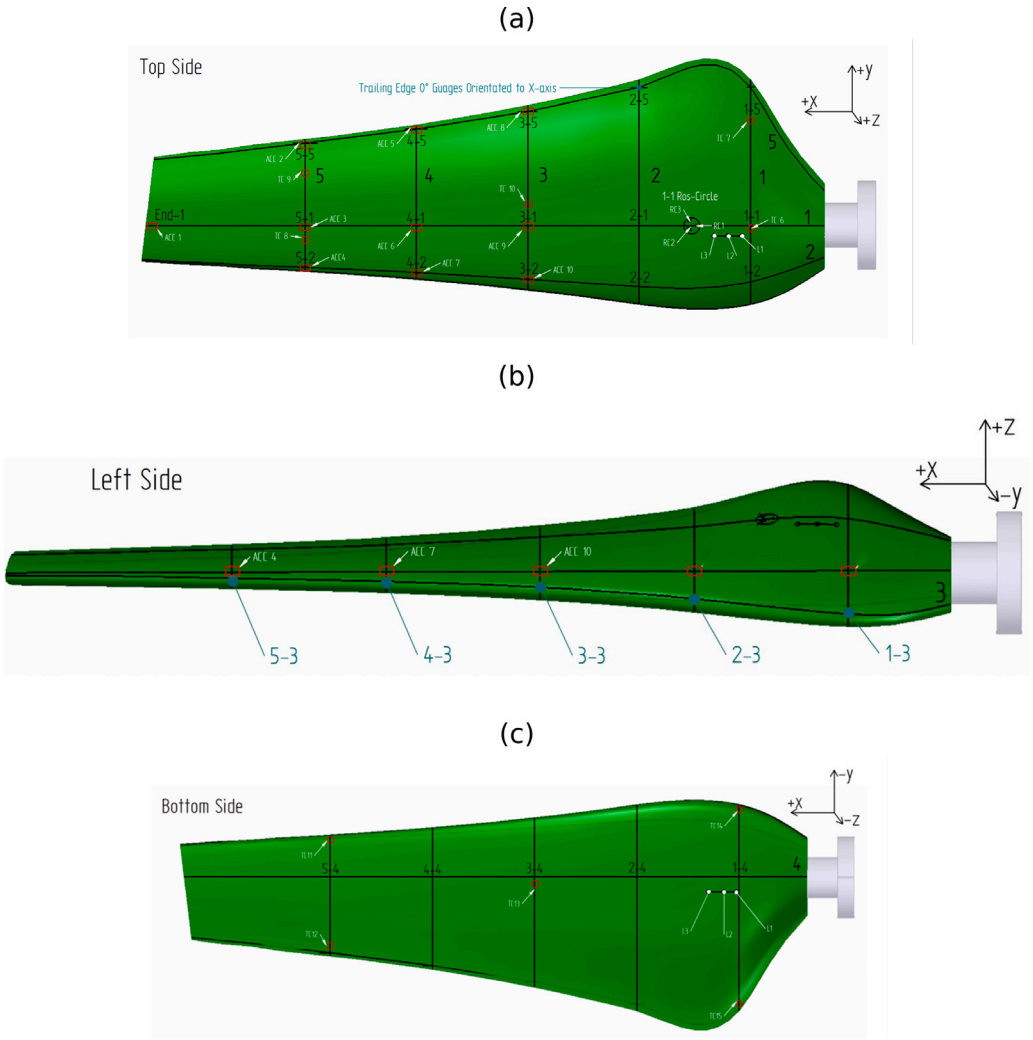

Fig. 4. Blade's sensor location. (a) The top side of the blade, (b) the lateral side of the blade, and (c) the bottom side of the blade.

relative variation in the edgewise RBMs was more pronounced due to their sensitivity to the angle of attack of the flow onto the blade. The maximum and minimum RBMs occurred at slightly different azimuthal positions from the top and bottom dead centre due to the interaction between the rotor-induced swirl velocity and the shear profile.

4.2. Static test

For all the tests, the loading and unloading phases both took 120 s each, and the target load was sustained for 3600 s. The displacement results for the centre and tip of the blade are presented in Table 3 for each of the tests. The 1st and 2nd static tests were conducted with a single actuator, while the 3rd and 4th were done with three actuators; for these last two tests, the total load value is obtained by the sum of the load in each single actuator, and all the actuators used the same load for this test.

Fig. 8 presents the strain variation results during the different static tests. In the figure, panel (a) is represented with an inverted axis to facilitate the comparison with the other two axes. The mean values are presented in the figure since the coefficient of variation (CV), which represents the ratio of the standard deviation concerning the mean, is low. The maximum values per panel are (a) −0.008 during the second test at cross-section 3, (b) 0.033 during the first test at cross-section 4, and panel (c) 3.229 during the first test at cross-section 4 followed by the second test with a value of −2.177 at cross-section 5.

Table 3
Displacement results from static tests.

Test	Load kN		RBM kN m.		Displacement centre mm		Displacement tip mm	
	mean	std	mean	std	mean	std	mean	std
1st static	267	0.08	952	0.30	30	0.18	123	1.00
2nd static	284	1.32	1014	4.71	29	0.07	114	0.56
3rd static	283	0.03	974	0.10	28	0.11	155	0.37
4th static	283	0.04	973	0.16	28	0.07	155	0.35

In Fig. 8 the panel (a), cross-section 1 shows similar strain values of the order of −600 με , and cross-section 2 has strains of the order of −2000 με, increasing to −2200 με at cross-section 3. However, the most significant difference is at cross-section 4, where in tests 3 and 4, the strain continues to rise slightly. In contrast, it decreases at different rates for the 1 and 2 tests. The decrease is clearly related to the position of the single actuator, and the difference in strain values between the first two tests is due to the movement of the actuator during the test. For the lateral left side of the blade (Fig. 8(b)), the first cross-section shows strain values of the order of 600 με, with slightly higher values during the first test. For the next two cross-sections, the first test shows values of around 50 με, higher than those for the other three tests, and, as in the case of the last cross-sections, there is a discrepancy between the single and multi-actuator tests, which can be interpreted in the same way as the ones in panel (a). Between the 1st and 2nd tests, the

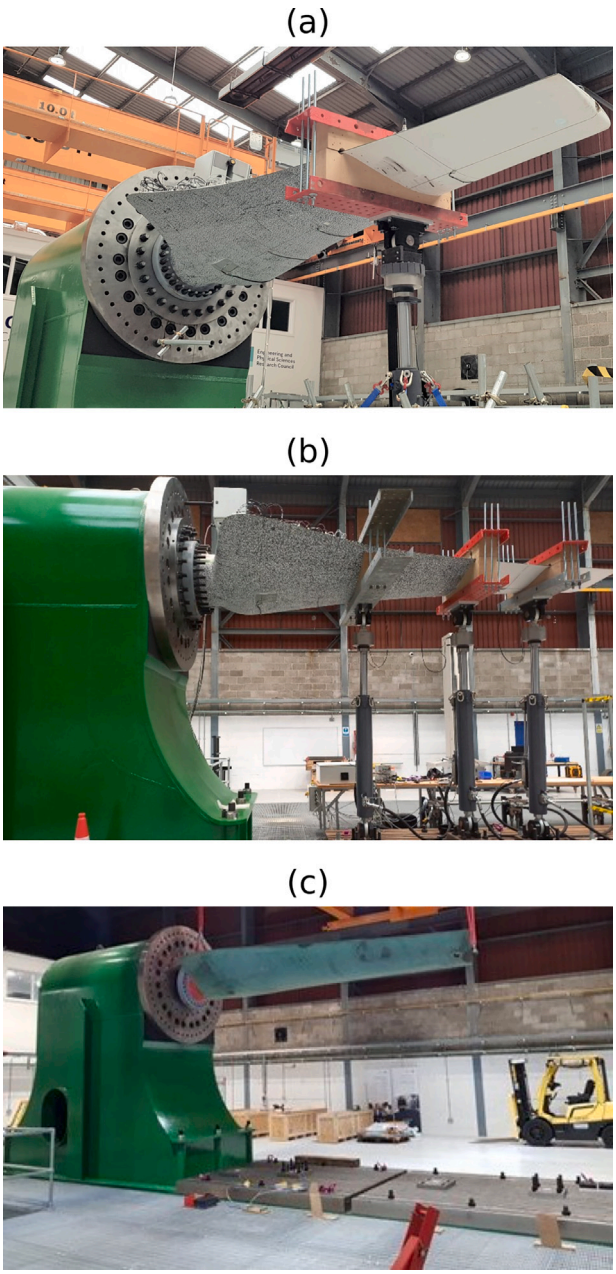

Fig. 5. Test configuration. (a) Single actuator; (b) Multiple actuators; and (c) No actuators.

strain gauge at cross-section four and longitudinal line 4 failed, and it was impossible to log that data for the following tests; this explains the appearance of the panel (c) in Fig. 8. In this case, it is interesting that similar values are presented in the first three cross-sections for all the tests, increasing from values of the order of 600 με in the first cross-section to 600 με in the third cross-section.

Moreover, cross-section 4 shows the highest values during the first test; nevertheless, this value seems out of range, and potentially, this could be due to a failure in the strain gauge. Additionally, the single actuator values are close to zero for the last stain gauge. In parallel, the multi-actuator test shows a strain of 1900 με, again showing how significant the difference in the number of actuators can be. Finally, the strain values during the 3rd and 4th tests, again, are for practical procedure overlap.

Table 4
Load, RBM and principal strains using a single actuator during fatigue tests.

Variable	Units	Mean	Crest	Trough	Amplitude
RBM	kN m.	363	646	93	553
Load	kN	102	181	26	155
Strain_1_1	mm/mm	−2.36E−04	−4.21E−04	−6.06E−05	−3.61E−04
Strain_2_1	mm/mm	−7.80E−04	−1.41E−03	−1.92E−04	−1.22E−03
Strain_3_1	mm/mm	−8.32E−04	−1.51E−03	−2.02E−04	−1.31E−03
Strain_4_1	mm/mm	−3.66E−04	−6.73E−04	−8.46E−05	−5.88E−04
Strain_1_3	mm/mm	2.12E−04	3.88E−04	4.68E−05	3.41E−04
Strain_2_3	mm/mm	2.50E−04	4.63E−04	4.98E−05	4.13E−04
Strain_3_3	mm/mm	3.03E−04	5.55E−04	6.82E−05	2.67E−08
Strain_4_3	mm/mm	2.14E−04	4.04E−04	3.37E−05	4.87E−04
Strain_1_4	mm/mm	2.26E−04	3.99E−04	6.22E−05	3.70E−04
Strain_2_4	mm/mm	8.94E−04	1.60E−03	2.29E−04	3.37E−04
Strain_3_4	mm/mm	9.57E−04	1.73E−03	2.36E−04	−1.49E−03
Strain_5_4	mm/mm	7.38E−06	6.68E−06	8.81E−06	−2.13E−06

4.3. Fatigue test

We carried out two fatigue tests, one between the first and second static tests and a second between the third and fourth static tests. On the first fatigue test, a total of 31 780 cycles, corresponding to 22.5 years of tidal cycles, were applied, and 30 485 cycles, corresponding to 21.6 years of tidal activity, were applied for the second test, while for both tests, the target RBM at the crest was 652 kN m. It should be noted that the test considers only the maximum RBM for a mean water velocity of 2.8 m/s and ignores the micro-load fluctuations during the rotation of the blades. During each test, the target number of cycles was 28 032 (approximately 20 years of tides); nevertheless, a series of extra cycles were carried out with the purpose of testing the facility's control system.

Table 4 presents the mean values of the load, RBM and principal strains during the single actuator tests, as well as the crest, the trough and the amplitude during a fatigue test using a single actuator. The data corresponds to the main axis for the longitudinal lines 1, 3 and 5 (see Fig. 4 and Table 2). The strain gauge at cross-section four and longitudinal line 4 failed during the first fatigue tests and has been removed. During the single actuator fatigue test, the strain CV at longitudinal line 1 was 0.43, occurring during the troughs of the cycles at cross-section 4, while during the crests, it was 0.003 at the same cross-section. For the longitudinal line 3, the maximum CV during the troughs occurred at cross-section 4 with a value of 1.020, and it took a value of 0.094 during crests at cross-section 4. Finally, for longitudinal line 4, the troughs report a CV value of 2.375 at cross-section 4, and the maximum CV during crests is 3.110 at cross-section 4.

Table 5 shows the corresponding data during a multi-actuator fatigue test. During the multi-actuator fatigue test, the CV at longitudinal line 1 was 0.504, occurring during the troughs of the cycles at cross-section 4, while during the crests, it was 0.004 at cross-section 1. For the longitudinal line 3, the maximum CV during the troughs was at cross-section 4 with a value of 0.512, while it took a value of 0.048 for crests at cross-section 2, and finally, for the longitudinal line 4, the troughs report a CV value of 0.565 at cross-section 4, and the corresponding maximum CV during crests is 0.035.

When we compare the values of Tables 4 and 5 during the crest for cross-section 1, longitudinal lines 1, 3 and 4 show lower values of the order of 12%, 3% and 6% during the single actuator test; meanwhile, cross-section 2 shows lower values of the order of 2%, 0% and 6%, and for cross-section 3, the values were lower: of the order of 9%, 7% and 8% for the longitudinal lines 1, 3 and 4. Finally, for cross-section 4, the values were lower by 141%, 60%, and 20 559% for the same longitudinal lines.

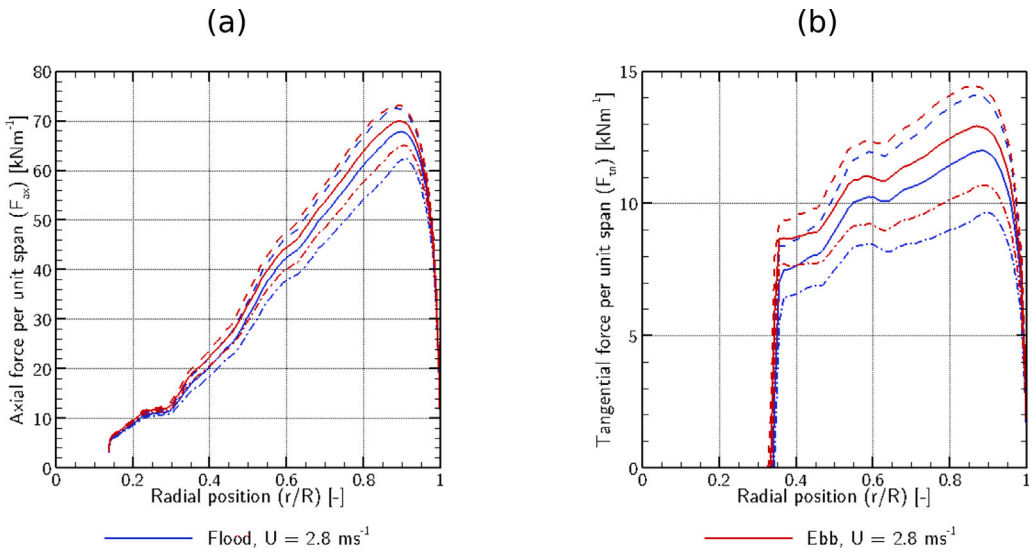

Fig. 6. Illustration of (a) the axial and (b) tangential blade loads along the span for both flood (blue) and ebb (red) tides at a flow speed of 2.8 m/s. The solid line represents the average load during a rotation, while the dashed and dash-dot lines indicate the minimum and maximum loads, respectively.

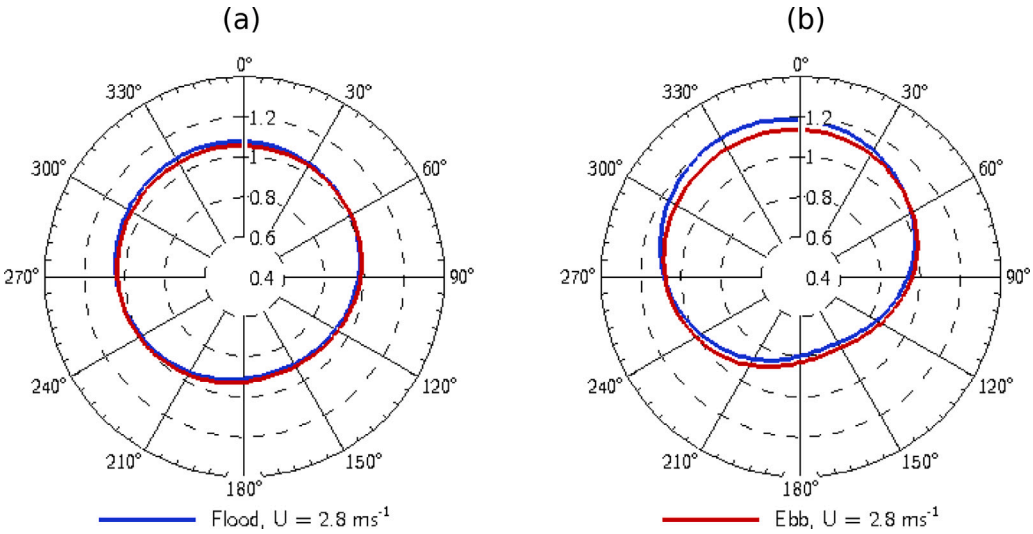

Fig. 7. Hydrodynamic simulation results. The azimuthal variation of the normalised blade root bending moments in (a) the flapwise and (b) edgewise directions is depicted for both flood (blue) and ebb (red) tides. The rotor operates at a hub-height flow speed of U = 2.8 m/s.

Table 5
Load, RBM and principal strains during fatigue tests using multi-actuators.

Variable	Units	Mean	Crest	Trough	Amplitude
RBM	kN m.	391	644	139	505
Load	kN	114	186	42	144
Strain_1_1	mm/mm	−2.67E−04	−4.72E−04	−5.82E−05	4.14E−04
Strain_2_1	mm/mm	−8.03E−04	−1.44E−03	−1.76E−04	1.26E−03
Strain_3_1	mm/mm	−9.03E−04	−1.65E−03	−1.70E−04	1.48E−03
Strain_4_1	mm/mm	−8.75E−04	−1.62E−03	−1.40E−04	1.48E−03
Strain_1_3	mm/mm	2.27E−04	4.01E−04	5.35E−05	3.48E−04
Strain_2_3	mm/mm	2.56E−04	4.64E−04	5.00E−05	4.14E−04
Strain_3_3	mm/mm	3.28E−04	5.93E−04	6.48E−05	5.28E−04
Strain_4_3	mm/mm	3.46E−04	6.48E−04	4.99E−05	5.98E−04
Strain_1_4	mm/mm	2.47E−04	4.24E−04	6.81E−05	3.56E−04
Strain_2_4	mm/mm	9.73E−04	1.70E−03	2.42E−04	1.46E−03
Strain_3_4	mm/mm	1.03E−03	1.86E−03	2.07E−04	1.65E−03
Strain_5_4	mm/mm	7.44E−04	1.38E−03	1.24E−04	1.26E−03

5. Discussion

Fig. 10 shows in a clearer way the differences in the bending moment and shear forces using a single or a multi-actuator test set-up. From the figures, the improvement in the distribution of the bending moments concerning the bending moment distribution obtained in the hydrodynamic simulations also shows how similar the RBM are for both cases, in agreement with Tables 3–5. Another significant aspect is the reduction in the shear force at a single point, as seen from Fig. 10; a single actuator has to exceed the target control shear force to match the RBM significantly and has a large step decrease. The repercussions of this effect have to be further investigated. Furthermore, no particular anomalies were detected during the present tests; this was confirmed by visual inspection of the data and using the system developed by [63]. The differences in the shear forces motivate the analysis of the influence of the clamping system used (see [63]) to ensure the fidelity of the stain gauge values close to the saddles, and further studies are under development to optimise the sensor placement [64].

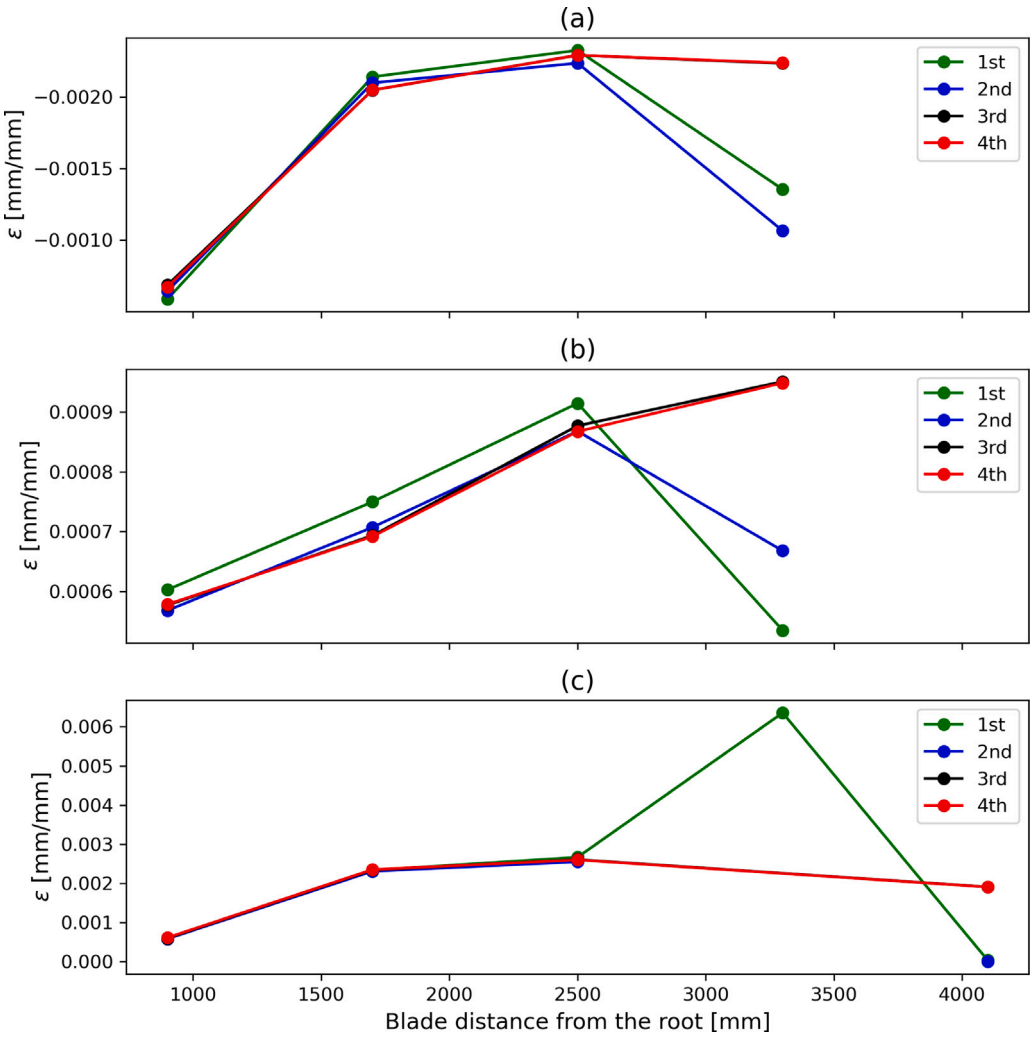

Fig. 8. Mean strain values during static tests. Green line for the 1st test (single actuator), blue line for the 2nd test (single actuator), black line for the 3rd test (multiactuator) and red line for the 4th test (multiactuator). Line locations (a) Longitudinal line 1; (b) Longitudinal line 3 and; (c) Longitudinal line 4.

5.1. Hydrodynamics

The data used in this work was obtained directly from the field, ensuring an accurate representation, at least for the specific site where this blade was deployed. Using a multi-actuator system can allow the testing of complex unsteady loads, which can significantly increase the loads acting on the blade relative to steady conditions [65]. This will require more effort in understanding which loads are meaningful to simulate and test, similar to the work done by [66] of classifying the water velocity profiles, including turbulence effects. Moreover, the introduction of an actuator close to the tip ensures a better understanding of the deflection of the blades near the tip, giving meaningful insights that can be used to calibrate the fluid–structure interactions modelling and obtain a better load distribution and energy production.

5.2. Static test

As mentioned in Section 4.2, the duration of the static test, once the target load was achieved, was 1 h; this value is based on the average duration of the maximum load during a tidal cycle. Moreover, according to IEC TS 62600-3:2020 A.8.3 [41] the blade should withstand the maximum load for the specified load duration or in the absence of a specific load duration (our case) a minimum of 30 s of the sustained static load is required. Based on these two statements and due to limitations in the use of the facility, the static test time was set to 1 h. Nevertheless, the IEC TS 62600-3:2020 A.8.3 [41] also recommend a minimum of 6 h of static load test for tidal energy converters and a comparison between a 6-hour test and 1-hour test is needed in future experiments. From the results in Table 3, we obtained a similar RBM using single or multiple actuators. Using a multi-actuator setup, we applied less load at any of the blade load contact points. At the same time, the displacement at the centre remained similar to those for the test with a single actuator and that with multiple actuators. Nevertheless, the tip behaviour changes, mainly due to the blade's internal structure. The blade has a metallic structural beam that runs half the length of the blade from the root, making the tip deflection highly sensitive to any load applied after the beam termination point. (see Section 3.1). It is worth mentioning that there were issues with the saddle system during the first static test. The system relies on the pressure and friction between the saddle and the blade. Nevertheless, this static test reports the saddle slipper in [42,43]. This could impact mainly the displacement results at the tip of the blade and can explain the size of the most significant standard deviation for the tip displacement. Overall, regarding the displacements and load introduction, we observe a low standard deviation in general, and the blade centre exhibits similar displacement, regardless of the multiple tests carried out.

5.3. Fatigue test

From the reported results, it is clear that the qualitative behaviour of the fatigue tests is in agreement with the behaviour of the static tests.

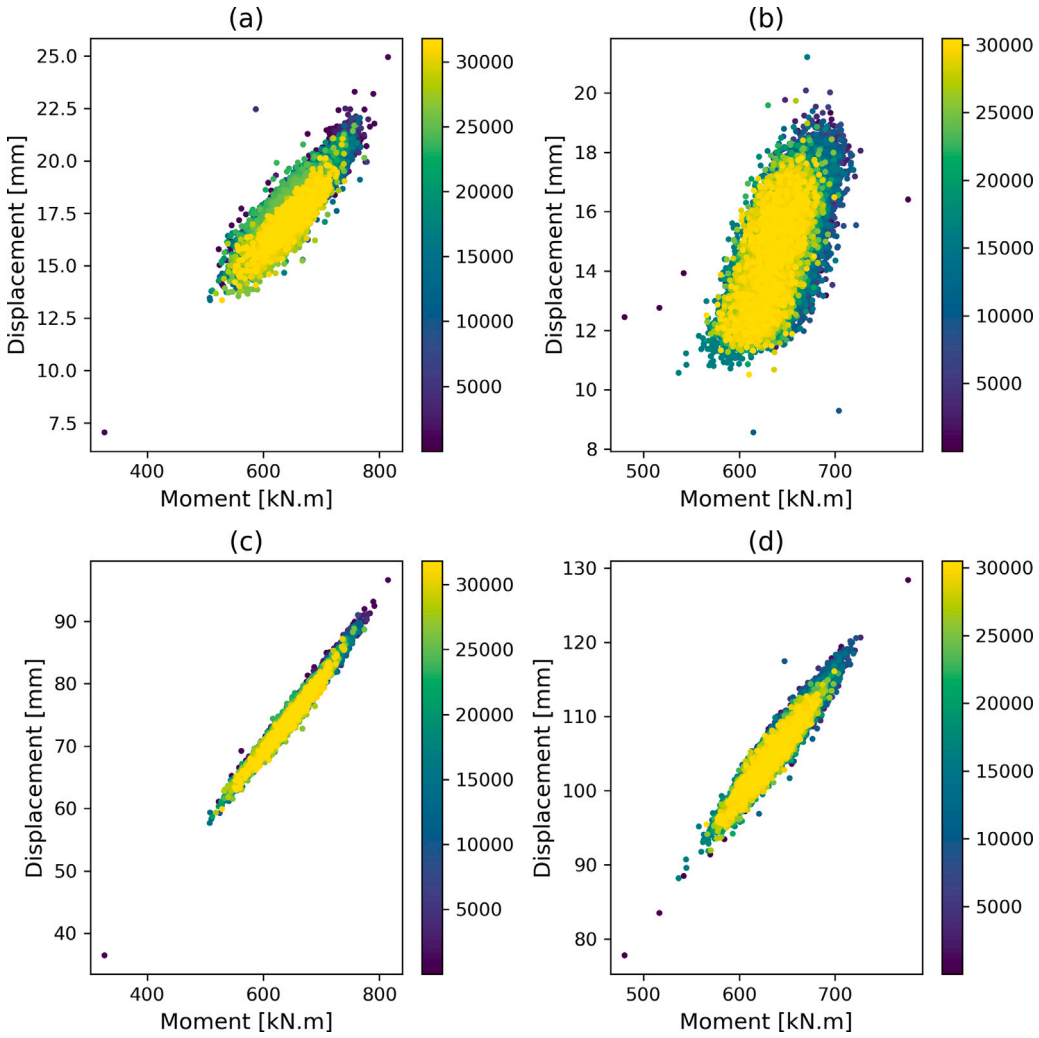

Fig. 9. Displacement against root bending moment during single and multi-actuator fatigue tests, where the colour bar refers to the number of cycles. (a) Single actuator fatigue test displacement refers to the centre of the blade, (b) Multi-actuator fatigue test displacement refers to the centre of the blade, (c) Single actuator fatigue test displacement refers to the tip of the blade, (d) Multi-actuator fatigue test displacement refers to the tip of the blade.

On average, the amplitude of the RBM was 5% higher, and the load amplitude was 7% higher for the single actuator test compared with that of the multi-actuator test. Nonetheless, there was no difference in the mean crest cycle values between the two actuator configurations. Regarding displacements (see Fig. 9), the second test was noisier and presented more outlier values in the initial cycles, but after that, the data seemed relatively compact and had an apparent linear behaviour. This noise increase is attributed to the use of more actuators, which could induce a more complex bending moment distribution around the blade. The control system is driven by load design control. Still, even if all the actuators target the same load and have targeted the same sine signal, they are each controlled independently so that even slight delays in the response of one of the actuators can cause complex moments or added noise across the blade. This effect is particularly more substantial at the blade's centre, which is between two actuators. At the same time, the displacements at the tip during the multi-actuator test show more variability due to the nearest actuator's proximity compared to the single-actuator test. Another notable behaviour is the displacement differences between tests; for the centre, the single actuator shows higher values, while for the tip, the higher values were recorded in the multi-actuator test. The load point actions can explain the differences; in the single test, all the loads were applied close to the centre, which is, therefore, expected to have higher displacements in this blade section. In the multi-actuator case, the tip displacement increased since a load was introduced at a section without the structural beam (thus more compliant to bending). Fig. 9(a) and (c) may suggest a change during the fatigue test; this behaviour is also seen in Fig. 11(a) and (c) but not in (b) and (d). This change seems to be an effect of the control system during the load introduction phase of the test rather than due to significant structural damage of the blade; this is supported by the information in Table 4, which does not show any significant change in the displacements before or after the fatigue tests. Nevertheless, we cannot discount the possibility of minor structural damages that may have occurred due to the fatigue tests.

It is worth remembering that for both tests, the main target was the RBM, which explains why the changes in the strain at the first two cross-sections are minimal and of the same order as the change in the RBM and the total load applied, and this is illustrated by Fig. 9. At the same time, as we move away from these two cross-sections, we can see a significant increase in strain variation, especially for cross-section 4. Even if it does not have a structural beam embedded, a structural failure in this region will completely change the hydrodynamics of the blade, leading to new moment distribution and the possible development of uneven loads on the rotor, potentially causing the failure or malfunction of the tidal turbine, representing a fundamental design failure of the blade.

This work focused on the principal load component during a tide for the Fatigue test, and future tests should encompass additional fatigue

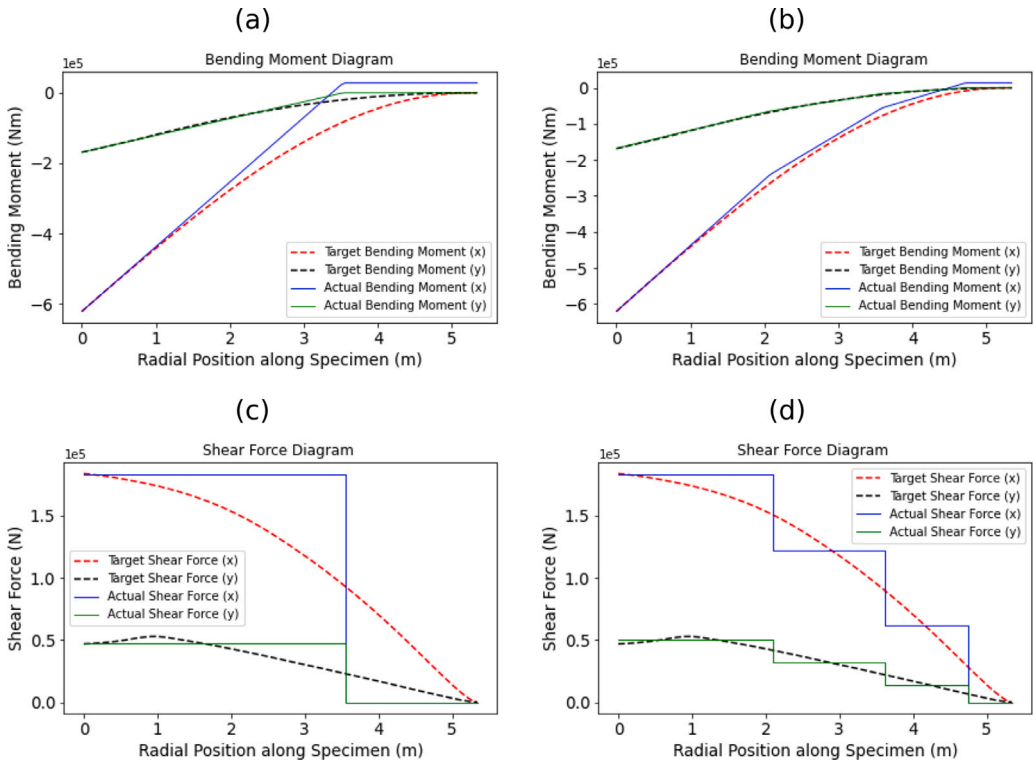

Fig. 10. Comparison of desired and applied bending moments and shear forces using single and multi-actuator fatigue tests. (a) Bending moments for a single actuator test, (b) Bending moments for the multi-actuator test, (c) Shear forces for the single actuator test, (d) Shear forces for the multi-actuator test.

variables, as discussed in Section 4.3. The current analysis did not include factors such as the rotational motion of the blade (see Fig. 7) and the impact of turbulence or wave interaction. To take into account the rotational effect, extra fatigue cycles with lower amplitude should be applied. The blade's operational speed is 13.78 rpm, and assuming it operates for only half of a flood or ebb cycle, then in 20 years, it will perform approximately 7.22E + 07 cycles. The rotational effect, notably prominent during the flood phase, exhibits varying intensities in both the edgewise and flapwise directions. In the edgewise direction, this effect peaks at 1.16 times the mean RBM, resulting in an RBM amplitude of 101 kN A m, while reaching a minimum of 0.8 times the RBM, generating an RBM amplitude of 126 kN A m. Conversely, in the flapwise direction, the rotational effect achieves a maximum of 1.07 times the mean RBM, resulting in an RBM amplitude of 11 kN A m, with minimum values at 0.9 times the RBM, yielding an RBM amplitude of 16 kN A m.

6. Conclusions

In this work, we successfully show and analyse the differences between single- or multi-actuator-driven static and fatigue mechanical tests of a full-scale (5.25 m) composite tidal blade. These were done at the new FastBlade fatigue test centre with its new digital displacement pumps, which are capable of recovering energy during fatigue tests. Besides opening new research venues (i.e., studies of clamping system anomalies), this research reveals a series of valuable lessons.

- Even for a similar root bending moment, there are clear differences in the moment distribution across the blade between the single and multi-actuator tests; this is reflected in the differing displacement and strain values along and across the blade (i.e., higher tip displacement, less shear stress in a single point).
- The use of multiple actuators allows a better representation of the distribution of loads and moments across the blade and the test of complex loads (i.e., the combination of pushing and pulling with different loads) that can better mimic effects such as turbulence, allowing more realistic tests.
- Even if the use of multiple actuators reduces the risk of overloading the specimen at a single point, as the shear stress diagrams show, it also affects the area for which measures can be taken due to the introduction of pre-stresses related to the load introduction systems. This means that an optimum balance in the number of load introduction points should be investigated.
- A multi-actuator test allows the introduction of a load close to the tip of the blade; this is particularly important, as it allows testing of a region of the blade that normally does not have additional structural support (i.e., by an embedded structural beam).
- There is a noise increase in the readings during a multi-actuator test setup, as reflected in the increased variance of displacement and strain readings; this effect is mainly due to a more complex load introduction system that increases control system delays due to less synchronicity between the separate actuator control loops.
- During all the tests performed on the blade, there was no significant damage or significant changes in the strain or displacement behaviour of the blade. Moreover, all the data suggested that the blade (as a whole system) retained its elastic behaviour.

The results of this research provide significant insight for tidal blade designers, manufacturers and regulatory bodies so that they can gauge the effectiveness of current design safety factors and design methodologies for their blades. This should lead to step-change improvements in blade design and testing, which should result in more efficient next-generation tidal turbine blades. This should result in more resilient, lower-cost blades with lower operation and maintenance costs, thus reducing the cost of tidal energy.

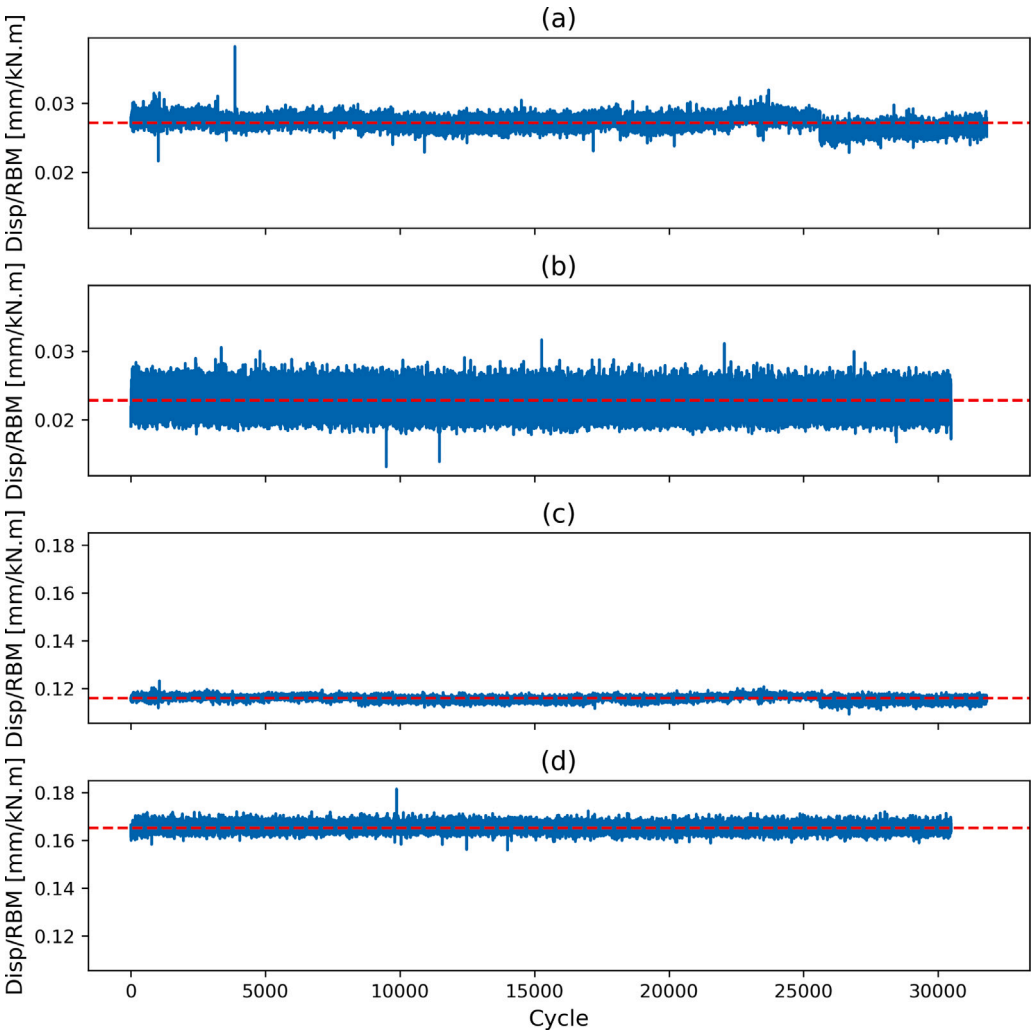

Fig. 11. Relation between displacement and root bending moment per cycle during single and multi-actuator fatigue tests, where the red dotted line refers to the mean value. (a) Single actuator fatigue test displacement refers to the centre of the blade, (b) Multi-actuator fatigue test displacement refers to the centre of the blade, (c) Single actuator fatigue test displacement refers to the tip of the blade, (d) Multi-actuator fatigue test displacement refers to the tip of the blade.

CRediT authorship contribution statement

Sergio Lopez Dubon: Writing – review & editing, Writing – original draft, Visualization, Validation, Supervision, Software, Methodology, Investigation, Formal analysis, Data curation, Conceptualization. **Fergus Cuthill:** Writing – original draft, Validation, Resources, Data curation, Conceptualization. **Christopher Vogel:** Writing – review & editing, Writing – original draft, Validation, Investigation, Formal analysis, Data curation. **Conchur Ó Brádaigh:** Writing – review & editing, Writing – original draft, Supervision, Formal analysis, Conceptualization. **Edward D. McCarthy:** Writing – review & editing, Writing – original draft, Supervision, Project administration, Funding acquisition, Formal analysis, Conceptualization.

Declaration of competing interest

The authors declare that they have no known competing financial interests or personal relationships that could have appeared to influence the work reported in this paper.

Data availability

Data will be made available on request.

Acknowledgements

The first author acknowledges the support from the European Union's Horizon 2020 research and innovation programme under the Marie Sklodowska-Curie grant agreement No. 801215 and the University of Edinburgh Data-Driven Innovation programme, part of the Edinburgh and South East Scotland City Region Deal.

CRV acknowledges the support of the UKRI through his Future Leaders Fellowship MR/V02504X/1.

All authors: The authors also wish to thank the Supergen ORE Hub for funding received through the Flexible Fund Award FF2020-1063.

References

[1] Waters S, Aggidis G. Tidal range technologies and state of the art in review. Renew Sustain Energy Rev 2016;59:514–29. http://dx.doi.org/10.1016/j.rser.2015.12.347.

[2] Adcock TAA, Draper S, Willden RHJ, Vogel CR. The fluid mechanics of tidal stream energy conversion. Annu Rev Fluid Mech 2021;53:287–310.

[3] Liu Y, Li Y, He F, Wang H. Comparison study of tidal stream and wave energy technology development between China and some western countries. Renew Sustain Energy Rev 2017;76:701–16. http://dx.doi.org/10.1016/j.rser.2017.03.049.

[4] Owen A. Tidal current energy: Origins and challenges. Future Energy: Improv, Sustain Clean Options Planet 2020;357–74. http://dx.doi.org/10.1016/B978-0-08-102886-5.00017-7.

[5] Liu H, Bahaj AS. Status of marine current energy conversion in China. Int Mar Energy J 2021;4(1):11–23. http://dx.doi.org/10.36688/IMEJ.4.11-23.

[6] Jeffrey H, Pennock S, Villate JL, Ruiz-Minguela P, Cagney D, Pirttimaa L. A European ocean energy industry – the €140bn economic opportunity. 2022, p. 1–28, URL https://www.etipocean.eu/knowledge_hub/industrial-roadmap-for-ocean-energy/.

[7] Grogan DM, Leen SB, Kennedy CR, Brádaigh CMÓ. Design of composite tidal turbine blades. Renew Energy 2013;57:151–62. http://dx.doi.org/10.1016/J.RENENE.2013.01.021.

[8] Kennedy CR, Leen SB, Brádaigh CM. A preliminary design methodology for fatigue life prediction of polymer composites for tidal turbine blades 2016;226:203–218 http://dx.doi.org/10.1177/1464420712443330 URL https://journals.sagepub.com/doi/10.1177/1464420712443330.

[9] Kennedy CR, Jaksic V, Leen SB, Brádaigh CM. Fatigue life of pitch- and stall-regulated composite tidal turbine blades. Renew Energy 2018;121:688–99. http://dx.doi.org/10.1016/J.RENENE.2018.01.085.

[10] Evans S. Analysis: Record-low price for UK offshore wind is nine times cheaper than gas - Carbon Brief, URL https://www.carbonbrief.org/analysis-record-low-price-for-uk-offshore-wind-is-four-times-cheaper-than-gas/.

[11] Jeffcoate P, Starzmann R, Elsaesser B, Scholl S, Bischoff S. Field measurements of a full scale tidal turbine. Int J Mar Energy 2015;12:3–20. http://dx.doi.org/10.1016/j.ijome.2015.04.002.

[12] Lake T, Hughes J, Togneri M, Williams AJ, Jeffcoate P, Starzmann R, Kaufmann N, Masters I. Strain gauge measurements on a full scale tidal turbine blade. Renew Energy 2021;170:985–96. http://dx.doi.org/10.1016/j.renene.2021.01.137.

[13] Zhang J, Zhang C, Angeloudis A, Kramer SC, He R, Piggott MD. Interactions between tidal stream turbine arrays and their hydrodynamic impact around Zhoushan Island, China. Ocean Eng 2022;246:110431. http://dx.doi.org/10.1016/J.OCEANENG.2021.110431.

[14] Huang B, Kanemoto T. Multi-objective numerical optimization of the front blade pitch angle distribution in a counter-rotating type horizontal-axis tidal turbine. Renew Energy 2015;81:837–44. http://dx.doi.org/10.1016/j.renene.2015.04.008.

[15] Abutunis A, Hussein R, Chandrashekhara K. A neural network approach to enhance blade element momentum theory performance for horizontal axis hydrokinetic turbine application. Renew Energy 2019;136:1281–93. http://dx.doi.org/10.1016/j.renene.2018.09.105.

[16] Saidi L, Benbouzid M, Diallo D, Amirat Y, Elbouchikhi E, Wang T. Higher-order spectra analysis-based diagnosis method of blades biofouling in a PMSG driven tidal stream turbine. Energies 2020;13(11):2888. http://dx.doi.org/10.3390/en13112888, URL https://www.mdpi.com/1996-1073/13/11/2888.

[17] Alipour RR, Alipour RR, Rahimian Koloor SS, Petrů M, Ghazanfari SA. On the performance of small-scale horizontal axis tidal current turbines. Part 1: One single turbine. Sustainability 2020;12(15):5985. http://dx.doi.org/10.3390/su12155985, URL https://www.mdpi.com/2071-1050/12/15/5985.

[18] Patel V, Eldho TI, Prabhu SV. Experimental investigations on Darrieus straight blade turbine for tidal current application and parametric optimization for hydro farm arrangement. Int J Mar Energy 2017;17:110–35. http://dx.doi.org/10.1016/J.IJOME.2017.01.007.

[19] Bahaj AS, Molland AF, Chaplin JR, Batten WM. Power and thrust measurements of marine current turbines under various hydrodynamic flow conditions in a cavitation tunnel and a towing tank. Renew Energy 2007;32(3):407–26. http://dx.doi.org/10.1016/J.RENENE.2006.01.012.

[20] Galloway PW, Myers LE, Bahaj ASBS. Quantifying wave and yaw effects on a scale tidal stream turbine. Renew Energy 2014;63:297–307. http://dx.doi.org/10.1016/j.renene.2013.09.030, URL https://linkinghub.elsevier.com/retrieve/pii/S0960148113004977.

[21] Walker JM, Flack KA, Lust EE, Schultz MP, Luznik L. Experimental and numerical studies of blade roughness and fouling on marine current turbine performance. Renew Energy 2014;66:257–67. http://dx.doi.org/10.1016/j.renene.2013.12.012, URL https://linkinghub.elsevier.com/retrieve/pii/S0960148113006769.

[22] JO C-h, LEE K-h. Application of an airfoil to the tidal turbine design by analyzing two-dimensional performance in the water. DEStech Trans Environ, Energy Earth Sci 2017;(eesd). http://dx.doi.org/10.12783/dteees/eesd2017/11988, URL http://dpi-proceedings.com/index.php/dteees/article/view/11988.

[23] Wang B-zz, Hu T-yy, Guo Y, Zhang Y-ff. Research on pitch control strategies of horizontal axis tidal current turbine. China Ocean Eng 2020;34(2):223–31. http://dx.doi.org/10.1007/s13344-020-0021-9, URL http://link.springer.com/10.1007/s13344-020-0021-9.

[24] McNaughton J, Ettema S, Zilic de Arcos F, Vogel CR, Willden RHJ. An experimental investigation of the influence of inter-turbine spacing on the loads and performance of a co-planar tidal turbine fence. J Fluids Struct 2023;118:103844.

[25] Guo B, Wang D, Zhou J, Shi W, Zhou X. Performance evaluation of a submerged tidal energy device with a single mooring line. Ocean Eng 2020;196:106791. http://dx.doi.org/10.1016/J.OCEANENG.2019.106791.

[26] Wang P, Zhao B, Cheng H, Huang B, He W, Zhang Q, Zhu F. Study on the performance of a 300W counter-rotating type horizontal axis tidal turbine. Ocean Eng 2022;255:111446. http://dx.doi.org/10.1016/J.OCEANENG.2022.111446.

[27] Shi W, Atlar M, Norman R, Aktas B, Turkmen S. Numerical optimization and experimental validation for a tidal turbine blade with leading-edge tubercles. Renew Energy 2016;96:42–55. http://dx.doi.org/10.1016/j.renene.2016.04.064, URL https://linkinghub.elsevier.com/retrieve/pii/S0960148116303664.

[28] Shi W, Rosli R, Atlar M, Norman R, Wang D, Yang W. Hydrodynamic performance evaluation of a tidal turbine with leading-edge tubercles. Ocean Eng 2016;117:246–53. http://dx.doi.org/10.1016/j.oceaneng.2016.03.044, URL https://linkinghub.elsevier.com/retrieve/pii/S0029801816300221.

[29] wei Zhu F, Ding L, Huang B, Bao M, Liu JT, Zhu Fw, Ding L, Huang B, Bao M, Liu JT. Blade design and optimization of a horizontal axis tidal turbine. Ocean Eng 2020;195:106652. http://dx.doi.org/10.1016/j.oceaneng.2019.106652.

[30] Wei X, Huang B, Liu P, Kanemoto T, Wang L. Experimental investigation into the effects of blade pitch angle and axial distance on the performance of a counter-rotating tidal turbine. Ocean Eng 2015;110:78–88. http://dx.doi.org/10.1016/j.oceaneng.2015.10.010, URL https://linkinghub.elsevier.com/retrieve/pii/S0029801815005478.

[31] Huang B, Usui Y, Takaki K, Kanemoto T. Optimization of blade setting angles of a counter-rotating type horizontal-axis tidal turbine using response surface methodology and experimental validation. Int J Energy Res 2016;40(5):610–7. http://dx.doi.org/10.1002/er.3383, URL http://doi.wiley.com/10.1002/er.3383.

[32] Sun ZC, Mao YF, Fan MH. Performance optimization and investigation of flow phenomena on tidal turbine blade airfoil considering cavitation and roughness. Appl Ocean Res 2021;106:102463. http://dx.doi.org/10.1016/J.APOR.2020.102463.

[33] Sutherland DR, Noble DR, Steynor J, Davey T, Bruce T. Characterisation of current and turbulence in the FloWave ocean energy research facility. Ocean Eng 2017;139:103–15. http://dx.doi.org/10.1016/j.oceaneng.2017.02.028.

[34] Draycott S, Nambiar A, Sellar B, Davey T, Venugopal V. Assessing extreme loads on a tidal turbine using focused wave groups in energetic currents. Renew Energy 2019;135:1013–24. http://dx.doi.org/10.1016/j.renene.2018.12.075.

[35] Draycott S, Payne GS, Steynor J, Nambiar A, Sellar B, Davey T, Noble DR, Venugopal V. Environmental & load data: 1:15 scale tidal turbine subject to a variety of regular wave conditions. Data in Brief 2019;23:103732. http://dx.doi.org/10.1016/J.DIB.2019.103732.

[36] Gaurier B, Druault P, Ikhennicheu M, Germain G. Experimental analysis of the shear flow effect on tidal turbine blade root force from three-dimensional mean flow reconstruction. Phil Trans R Soc A 2020;378(2178):20200001. http://dx.doi.org/10.1098/rsta.2020.0001, URL https://royalsocietypublishing.org/doi/10.1098/rsta.2020.0001.

[37] Martinez R, Gaurier Bt, Ordonez-Sanchez S, Facq JV, Germain G, Johnstone C, Santic I, Salvatore F, Davey T, Old C, Sellar BG. Tidal energy round robin tests: A comparison of flow measurements and turbine loading. J Mar Sci Eng 2021;9(4):425. http://dx.doi.org/10.3390/JMSE9040425, 2021, Vol. 9, Page 425 URL https://www.mdpi.com/2077-1312/9/4/425/htm https://www.mdpi.com/2077-1312/9/4/425.

[38] McNaughton J, Cao B, Nambiar A, Davey T, Vogel CR, Willden RHJ. Constructive interference effects for tidal turbine rotors. J Fluid Mech 2022;943:A38.

[39] Badoe CE, Edmunds M, Williams AJ, Nambiar A, Sellar B, Kiprakis A, Masters I. Robust validation of a generalised actuator disk CFD model for tidal turbine analysis using the FloWave ocean energy research facility. Renew Energy 2022;190:232–50. http://dx.doi.org/10.1016/J.RENENE.2022.03.109.

[40] de la Torre O, Moore D, Gavigan D, Goggins J. Accelerated life testing study of a novel tidal turbine blade attachment. Int J Fatigue 2018;114:226–37. http://dx.doi.org/10.1016/J.IJFATIGUE.2018.05.029.

[41] Institution BS. Marine energy. Wave, tidal and other water current converters. Part 3, measurement of mechanical loads. 2020, URL https://www.document-center.com/standards/show/PD-IEC-62600-3.

[42] Dubon SL, Vogel C, a DC, nd E. McCarthy FC. Fastblade: A technological facility for full-scale tidal fatigue testing. In: SAMPE 2023. 2023, http://dx.doi.org/10.33599/NASAMPE/S.23.0062, URL https://www.nasampe.org/store/viewproduct.aspx?id=22014036.

[43] Dubon SL, Vogel CR, Cava DG, Cuthill F, McCarthy ED, Bradaigh CMÓ. Fastblade: A technological facility for full-scale tidal blade fatigue testing. SSRN 2023. http://dx.doi.org/10.2139/SSRN.4400928, URL https://papers.ssrn.com/abstract=4400928.

[44] Dubon SL, Vogel C, Cava DG, Cuthill F, McCarthy E, Bradaigh CO. Multi-actuator full-scale fatigue test of a tidal blade. In: Proceedings of the european wave and tidal energy conference. vol. 15, 2023, http://dx.doi.org/10.36688/ewtec-2023-177.

[45] Glennon C, Finnegan W, Kaufmann N, Meier P, Jiang Y, Starzmann R, Goggins J. Tidal stream to mainstream: mechanical testing of composite tidal stream blades to de-risk operational design life. J Ocean Eng Mar Energy 2022;8:163–82. http://dx.doi.org/10.1007/S40722-022-00223-4/FIGURES/23, URL https://link.springer.com/article/10.1007/s40722-022-00223-4.

[46] DNV. Tidal turbines. DNV standard. DNVGL-ST-0164. 2015, URL https://www.dnv.com/energy/standards-guidelines/dnv-st-0164-tidal-turbines.html.

[47] Finnegan W, Jiang Y, Meier P, Hung LC, Fagan E, Wallace F, Glennon C, Flanagan M, Flanagan T, Goggins J. Numerical modelling, manufacture and structural testing of a full-scale 1 MW tidal turbine blade. Ocean Eng 2022;266:112717. http://dx.doi.org/10.1016/j.oceaneng.2022.112717, URL https://www.sciencedirect.com/science/article/pii/S0029801822020005.

[48] Thanthirige TRM, Goggins J, Flanagan M, Finnegan W. A state-of-the-art review of structural testing of tidal turbine blades. Energies 2023;16:4061. http://dx.doi.org/10.3390/EN16104061, 2023, Vol. 16, Page 4061 URL https://www.mdpi.com/1996-1073/16/10/4061/htm https://www.mdpi.com/1996-1073/16/10/4061.

[49] Sellar B. Metocean data set from the ReDAPT tidal project: Batch 1, part 2, 2011–2014 [dataset]. 2015, http://dx.doi.org/10.7488/ds/1687.

[50] Sellar B, Sutherland D. Tidal energy site characterisation at the fall of warness, EMEC, UK. 2016, URL https://tethys.pnnl.gov/publications/tidal-energy-site-characterisation-fall-warness-emec-uk.

[51] Sellar BG, Wakelam G, Sutherland DR, Ingram DM, Venugopal V. Characterisation of tidal flows at the european marine energy centre in the absence of ocean waves. Energies 2018;11. http://dx.doi.org/10.3390/EN11010176.

[52] Ahmed U, Apsley D, Afgan I, Stallard T, Stansby P. Fluctuating loads on a tidal turbine due to velocity shear and turbulence: Comparison of CFD with field data. Renew Energy 2017;112:235–46. http://dx.doi.org/10.1016/j.renene.2017.05.048, URL https://www.sciencedirect.com/science/article/pii/S0960148117304330.

[53] Menter FR, Kuntz M, Langtry R. Ten years of industrial experience with the SST turbulence model. Turbul, Heat Mass Transf 2003;4. URL http://aaac.larc.nasa.gov/tsab/cfdlarc/aiaa-dpw/.

[54] Wimshurst A, Willden RH. Analysis of a tip correction factor for horizontal axis turbines. Wind Energy 2017;20:1515–28. http://dx.doi.org/10.1002/WE.2106.

[55] Schluntz J, Willden RH. An actuator line method with novel blade flow field coupling based on potential flow equivalence. Wind Energy 2015;18:1469–85. http://dx.doi.org/10.1002/WE.1770.

[56] Shen WZ, Sørensen JN, Mikkelsen R. Tip loss correction for actuator/Navier–Stokes computations. J Sol Energy Eng 2005;127:209–13. http://dx.doi.org/10.1115/1.1850488, URL https://asmedigitalcollection.asme.org/solarenergyengineering/article/127/2/209/461527/Tip-Loss-Correction-for-Actuator-Navier-Stokes.

[57] Apsley DD, Stallard T, Stansby PK. Actuator-line CFD modelling of tidal-stream turbines in arrays. J Ocean Eng Mar Energy 2018;4:259–71. http://dx.doi.org/10.1007/S40722-018-0120-3/FIGURES/17, URL https://link.springer.com/article/10.1007/s40722-018-0120-3.

[58] Negru I, Gillich GR, Praisach ZI, Tufoi M, Gillich N. Natural frequency changes due to damage in composite beams. J Phys Conf Ser 2015;628:012091. http://dx.doi.org/10.1088/1742-6596/628/1/012091, URL https://iopscience.iop.org/article/10.1088/1742-6596/628/1/012091 https://iopscience.iop.org/article/10.1088/1742-6596/628/1/012091/meta.

[59] QBlade documentation — qblade documentation 2.0.6.4 documentation, URL https://docs.qblade.org/.

[60] Larson C, Brooks C, Hill S, Sproles D. Computer program to obtain ordinates for NACA airfoils. 1996.

[61] Huxley-Reynard C, Thake J, Gibberd G. TG-RE-040-0091 Rev B deepgen blade design report. 2008.

[62] Huxley-Reynard C, King J, Gibberd G. TG-RE-000-0081 Rev D extreme and fatigue load calculations for deepgen 500kw tidal turbine. 2008.

[63] Camacho MAV, Munko M, Cuthill F, Brádaigh CMÓ, McCarthy E, Dubon SL. Parasitic effects of load introduction points in full-scale composite tidal turbine blade tests. In: 60th annual british conference on non-destructive testing. 2023.

[64] McLoughlin J, Munko MJ, Camacho MA, Cuthill F, Lopez Dubon S. Use of digital image correlation and machine learning for the optimal strain placement in a full scale composite tidal turbine blade. In: Proceedings of the 19th international conference on condition monitoring and asset management. Northampton; 2023, http://dx.doi.org/10.1784/cm2023.2d4.

[65] Lam R, Dubon SL, Sellar B, Vogel C, Davey T, Steynor J. Temporal and spatial characterisation of tidal blade load variation for structural fatigue testing. Renew Energy 2023;208:665–78. http://dx.doi.org/10.1016/j.renene.2023.03.117, URL https://www.sciencedirect.com/science/article/pii/S0960148123004202.

[66] Lopez Dubon S, Valdivia Camacho M, Lam R, Sellar B. A machine learning approach for tidal flow classification. SSRN 2023. http://dx.doi.org/10.2139/ssrn.4446221, URL https://ssrn.com/abstract=4446221.